First NIR interferometrically resolved high order Brackett and forbidden Fe lines of a B[e] star: V921 Sco

Alexander Kreplin[1]★, Stefan Kraus[1], Larisa Tambovtseva[2], Vladimir Grinin[2,3], Edward Hone[1]

[1] *University of Exeter, Astrophysics Group, Stocker Road, Exeter, EX4 4QL, UK*
[2] *Pulkovo Observatory of RAS, Pulkovskoe shosse 65, St. Petersburg 196140, Russia*
[3] *The V.V. Sobolev Astronomical Institute of the St. Petersburg University, Petrodvorets, St. Petersburg 198904, Russia*

Accepted 2019 November 25. Received 2019 November 25; in original form 2019 October 18

ABSTRACT

We present near-infrared interferometric AMBER observations of the B[e] binary V921 Sco at low (R~30) and medium spectral resolution (R~1500) in the K- and H-bands. Low spectral resolution AMBER data were used to estimate the position of the companion V921 Sco B and confirmed a clockwise movement on sky with respect to the primary of 33° between 2008 and 2012. Our observations resolve for the first time higher order Brackett lines (Br6–Br12). The modelling of the different line transitions revealed a decrease in the size of the line-emitting regions from Br3–Br12. We are able to reproduce this decrease with a simple radiative transfer model of an equatorial disk in local thermodynamic equilibrium. In addition to the Brackett series, we also resolve permitted and forbidden Fe line emission. Our modelling shows that these lines originate from ~2au from the star, corresponding roughly to the measured dust sublimation region. This might indicate that the forbidden line emission arises from shock-excitation at the base of a disk wind.

Key words: circumstellar matter – stars: individual: V921 Sco – stars: formation – stars: pre-main-sequence – stars: emission-line, Be – techniques: interferometric

1 INTRODUCTION

Studying the accretion and outflow processes in young stars is of fundamental importance for improving our understanding of star and planet formation. Most of the circumstellar disk mass represents gas, in particular hydrogen, that can be traced by spectral lines. In the near-infrared (NIR), typical tracers are the Brackett (Br) lines (for Brγ see e.g. Muzerolle et al. 1998; Weigelt et al. 2006). A sub-class of intermediate-mass Be stars, the B[e] stars, show forbidden line emission. Forbidden line emission, first identified almost a century ago, has been repeatedly observed in the spectra of hot stars (e.g., Merrill 1928; Merrill & Burwell 1933; Allen & Swings 1976) and indicates the presence of a large amount of low-density, optically thin gas in the circumstellar environment. Remarkably, the occurrence of forbidden lines, e.g., [OI], [SII] and [Fe II] and the existence of a strong infrared excess seems to be strongly correlated (Swings 1977). Consequently, the ionised low-density gas must coexist with other circumstellar material which is dense and cold enough to form dust and which must be distributed in distinct non-spherically symmetric regions (Lamers 2006). The forbidden lines are expected to emerge at larger spatial scales than the thermal K-band continuum emission from dust (e.g., Davis et al. 2003; Gomez de Castro & Pudritz 1992). The high mass-loss rate and the occurrence of the large amount of low-density gas in B[e] stars might be triggered by a close companion, and therefore hints to a binary nature of B[e] stars in general (Miroshnichenko et al. 2007). The different hydrogen and iron lines are expected to originate from different regions of the circumstellar environment. Near-infrared interferometry provides a unique tool to investigate the different K- and H-band line-emitting regions in a circumstellar disk on small spatial scales.

One of the brightest stars showing the B[e]-phenomenon is V921 Sco. This Southern emission line star is an intermediate-mass object of spectral type B0 with a mass of ~8-10 $M_\odot$ (Borges Fernandes et al. 2007). The nature of V921 Sco is still under debate. In literature it has been been classified as a B[e] supergiant (Hutsemekers & van Drom 1990; Miroshnichenko et al. 1995; Borges Fernandes et al. 2007) but also appeared as a Herbig Be star (Arun et al. 2019; Henning et al. 1994; The et al. 1994; Mannings 1994). The discovery of a circumstellar disk as well as the presence of 26 stellar sources within 1 arcmin around V921 Sco (Kraus et al. 2012b), with many of them identified as

★ E-mail: a.kreplin@exeter.ac.uk

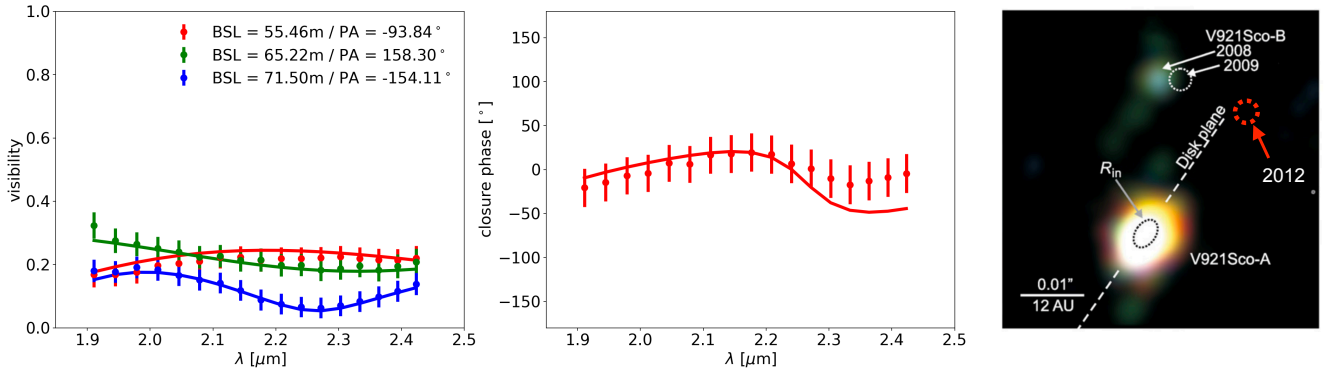

Figure 1. Geometric model fit of the AMBER 2012 LR visibilities (left) and closure phases (middle). The model consists of two point sources representing the central star and its companion, and a temperature-gradient disk centered around the primary. Whereas the parameters of the temperature-gradient disk were fixed to the values reported in Kraus et al. (2012c), the position of the companion was fitted. The right panel is a composite of the interferometric image from Kraus et al. (2012b) with the best-fit position for V921 Sco B overlayed (shown in red).

Table 1. Observation log of the VLTI/AMBER low-resolution (R~30) K-band and medium-resolution (R~1500) K- and H-band observations of V921 Sco.

Mode	UT Date	UT Time [hh:mm]	DIT [ms]	NDIT #	Telescopes	Proj. baselines [m]	PA [°]	Calibrator
LR-KH	2012-06-18	06:00–06:09	100	1000	D0-H0-G1	55.5 / 65.2 / 71.5	-86.2 / 21.7 / -25.9	HD 141687
MR-K	2012-06-01	02:29–02:35	200	200	UT2-UT3-UT4	46.6 / 52.3 / 82.7	-108.8 / 4.4 / 35.6	HD 104479
MR-H	2012-05-06	08:31–08:41	100	490	UT2-UT3-UT4	50.0 / 81.9 / 114.4	50.3 / -11.5 / 11.2	HD 152040
MR-H	2012-06-01	08:01–08:19	100	490	UT2-UT3-UT4	34.1 / 57.8 / 70.2	-154.2 / -58.0 / -29.1	HD 167768

embedded low- and intermediate mass YSOs (Habart et al. 2003), also hints to a young evolutionary stage. Using our 2008/2009 AMBER observations, we discovered that V921 Sco is indeed a binary system, consisting of the primary V921 Sco A and the close (25.0 ± 0.8 mas; $\sim 29 \pm 0.9$ AU at 1.15 kpc) companion V921 Sco B (Kraus et al. 2012b). The orbital period was estimated to be ~ 35 years (for a circular orbit). The orbital motion measured between two epochs in 2008 and 2009 was ~ 7° per year. The K and H band images clearly show a disk-like structure with indications for a radial temperature gradient. In this paper, we present new K- and H-band data of V921 Sco taken in 2012 at low- and medium-spectral resolution. In contrast to former studies, we present the first dispersed interferometric observations in H-band lines of V921 Sco.

In Section 2 we describe the observations and in Section 3 the geometric and LTE modelling. We present the results and the conclusion in Section 4 and 5.

2 OBSERVATIONS AND DATA REDUCTION

The B[e] star V921 Sco was observed in May and June 2012 in the H- and K-band (~ 1.6μm and ~ 2.2μm respectively) within the observing programs 089.C-0959 and 089.C-0563 with the near-infrared interferometric VLTI/AMBER instrument (Petrov et al. 2007; Tatulli et al. 2007). All data have been reduced using the AMBER data reduction library *amdlib*[1] version 3.0.9. For the 2012-06-18 low-resolution (LR) data, we applied the histogram-equalization method to reduce atmospheric optical-path-length biases in the calibrated products (for details please see Kreplin et al. 2012). From the LR and medium-resolution (MR) AMBER data, 20% with the best fringe-signal-to-noise ratio were selected for further processing and interpretation (Tatulli et al. 2007). Due to low signal-to-noise-ratio (S/R) in the MR AMBER data, we only considered data sets with a Root Mean Square (RMS)< 0.2 for each interferometric quantity (visibility, differential phase, closure phase, respectively). This lead in the H band to a total of four usable *uv*-positions for visibility extraction and two usable *uv*-positions for the extraction of a differential phase signal. In the K band, three *uv*-positions with usable visibilities and one *uv*-position with a reliable differential phase signal have been selected for further analysis. Whereas we could retrieve closure phase information for the LR AMBER data, no closure phase information could be extracted due to low S/R in all MR data sets. In the MR AMBER data, all spectral lines were identified using the NIST (National Institute of Standards and Technology) database[2] Kramida et al. (2018). Besides the hydrogen Br3 (Brγ) line at 2.166 μm we find in the spectrum of V921 Sco transitions ranging from Br6(at 1.737 μm)–Br12(at 1.556 μm) as shown in the top panels of Fig. 2 and in Table 2. The observing log is shown in Table 1.

[1] https://www.jmmc.fr/data_processing_amber.htm
[2] https://www.nist.gov/pml/atomic-spectra-database

3 MODELLING

Our study focuses on the modelling and interpretation of the origin of the hydrogen and permitted and forbidden Fe line. To be able to interpret the MR AMBER visibilities and phases within different spectral lines it is crucial to know the underlying spatial distribution of the continuum emission. Because V921 Sco is a binary system (Kraus et al. 2012b) we have to include the circumstellar environment of the primary and estimate the binary separation (SEP) and position angle (PA) at the date of observation. According to our former analysis of the system, the continuum consists of V921 Sco A hosting the circum-primary disk and the companion V921 Sco B. To derive the continuum geometry of the V921 Sco system, we used LR K-band AMBER data recorded near the date of the recording of the MR data (see Table 1). The circum-primary environment is described by a temperature-gradient disk model (TGM; e.g. Kreplin et al. 2012) with the parameters found in Kraus et al. (2012c). As the companion V921 Sco B moved already about 7° between the 2008 and 2009 epoch, we had to fit the new position near the epoch of our 2012 MR observations. The combined continuum visibility $V_{\rm cont}(u,v,\lambda)$ of the V921 Sco system can be written as

$$V_{\rm cont}(u,v,\lambda) = |\widetilde{V}_{\rm cont}(u,v,\lambda)| = \frac{|f_{\rm A}V_{\rm A} + f_{\rm B}V_{\rm B} + f_{\rm TGM}V_{\rm TGM}|}{f_{\rm A}+f_{\rm B}+f_{\rm TGM}}, \quad (1)$$

where $f_{\rm A}$, $f_{\rm B}$ and $f_{\rm TGM}$ denote the fluxes of the primary V921 Sco A, the secondary V921 Sco B and the circum-primary disk flux modeled by a TGM, respectively. The visibilities of the two unresolved stellar components $V_{\rm A}$ and $V_{\rm B}$ are set to unity. The two-dimensional visibility is a function of the Fourier coordinates u and v in the uv-plane as well as the wavelength λ. The model was constructed using our own developed modelling suite for interferometric data incorporating different fitting algorithms (Newville et al. 2014) as used in former projects (e.g. Kreplin et al. 2016, 2018). The position of the companion was fitted using a Monte-Carlo Markov Chain algorithm (*emcee*) to a separation SEP=23.5 ± 0.1mas (corresponding to a projected separation on the sky of ~26au at a distance of 1150pc) and a position angle PA=320.3 ± 0.3° The best fit can approximately reproduce not only the visibilities but also the closure phase of the LR AMBER data (see Fig. 1). The new position of V921 Sco B is plotted within the reconstructed near-infrared composite image (see Kraus et al. 2012c) in the right panel of Fig. 1.

3.1 Geometric models

For interpretation of the individual spectral lines we employ a geometric modelling approach for young stellar objects (YSOs) used in earlier studies (e.g. Kreplin et al. 2018). The continuum is described by Eqn. 1. The spatial geometry of the individual lines are modeled, for simplicity, as two-dimensional elliptical Gaussian components centered around the primary component V921 Sco A. The total visibility is described by

$$V_{\rm total}(u,v,\lambda) = \frac{|f_{\rm line}V_{\rm line} + f_{\rm cont}\widetilde{V}_{\rm cont}|}{f_{\rm line}+f_{\rm cont}}, \quad (2)$$

where $f_{\rm cont} = f_{\rm A}+f_{\rm B}+f_{\rm TGM}$ denotes the total continuum flux and $f_{\rm line}$ the flux within the line. The PA and axis ratio of the elliptical Gaussian component are fixed to the parameters derived by the continuum model of PA=55° and a/b=1.52, where a and b denote the semi-major and semi-minor axis, respectively (corresponding to an inclination of the system of 48.8°; Kraus et al. 2012b). The only free parameter is the Gaussian half-width-at-half-maximum (HWHM) that is denoted as η throughout this paper. Because of the low S/R of the differential phases, only visibilities have been used for fitting. Nevertheless, we show the corresponding differential phases of our best-fit model for comparison. Please note that although the Gaussian model is centro-symmetric, a non-zero differential phase is expected due to the complex continuum geometry. The model differential phase signals show a consistent trend towards the measured signals. The fit results are given in Table 2.

3.2 Radiative transfer model

We employ a simple radiative transfer model to compare the modelled emitting radii of the various hydrogen transitions to expected excitation structures in a typical circumstellar disk. The material is assumed to be in local thermodynamic equilibrium (LTE). Please note that the assumption of LTE might underestimate the line intensities in level populations where non-LTE effects might play a role. This depends strongly on the temperature and density of the emitting gas. The possible bias that might be introduced in the line intensity by the LTE assumption will change the interferometrically measured size of the line emitting region only marginally. Data with greater S/R and sophisticated non-LTE modeling will be required to analyse the gaseous circumstellar environment in detail. In our model, the material is located in an equatorial disk with a half-opening angle of 5°. The disk expands from the stellar surface at a constant vertical density per unit volume (for details please see Kraus et al. 2012a). The stellar parameters were adapted from Borges Fernandes et al. (2007), namely an effective temperature $T_{\rm eff} = 14000K$, a distance $d = 1150$pc, and a stellar radius $R = 17.3R_{\odot}$. We compute the emitting intensities per unit area and plot them as a function of radius r (see Fig. 3 left). To compare the relative emission size of the LTE model to our fitted HWHM we extracted the centroid position from the intensities shown in the left panel of Fig. 3 with the standard equation $x_{\rm centroid} = \sum[r\cdot I(r)]/\sum I(r)$. In the right panel in Fig. 3, we show a decrease of the emission size of the higher order Br6–Br12 transitions normalized to the emission size of Brγ (blue data points). Our LTE model shows a similar trend as seen in our observations (red curve), reproducing that the higher order Br-lines originate from a region more compact than the Brγ line emission region. More sophisticated modelling is needed to explore the detailed emission characteristic i.e. emission arising from a Keplerian disk or a disk wind, but this is out of the scope of this exploratory study.

4 RESULTS

With the LR AMBER data we derived for the companion V921 Sco B a separation of ~ 23mas (corresponding to a projected separation on the sky of ~ 26au at a distance of 1150pc) and a position angle of -40° for our new epoch in June 2012. The position angle difference of ~33° between

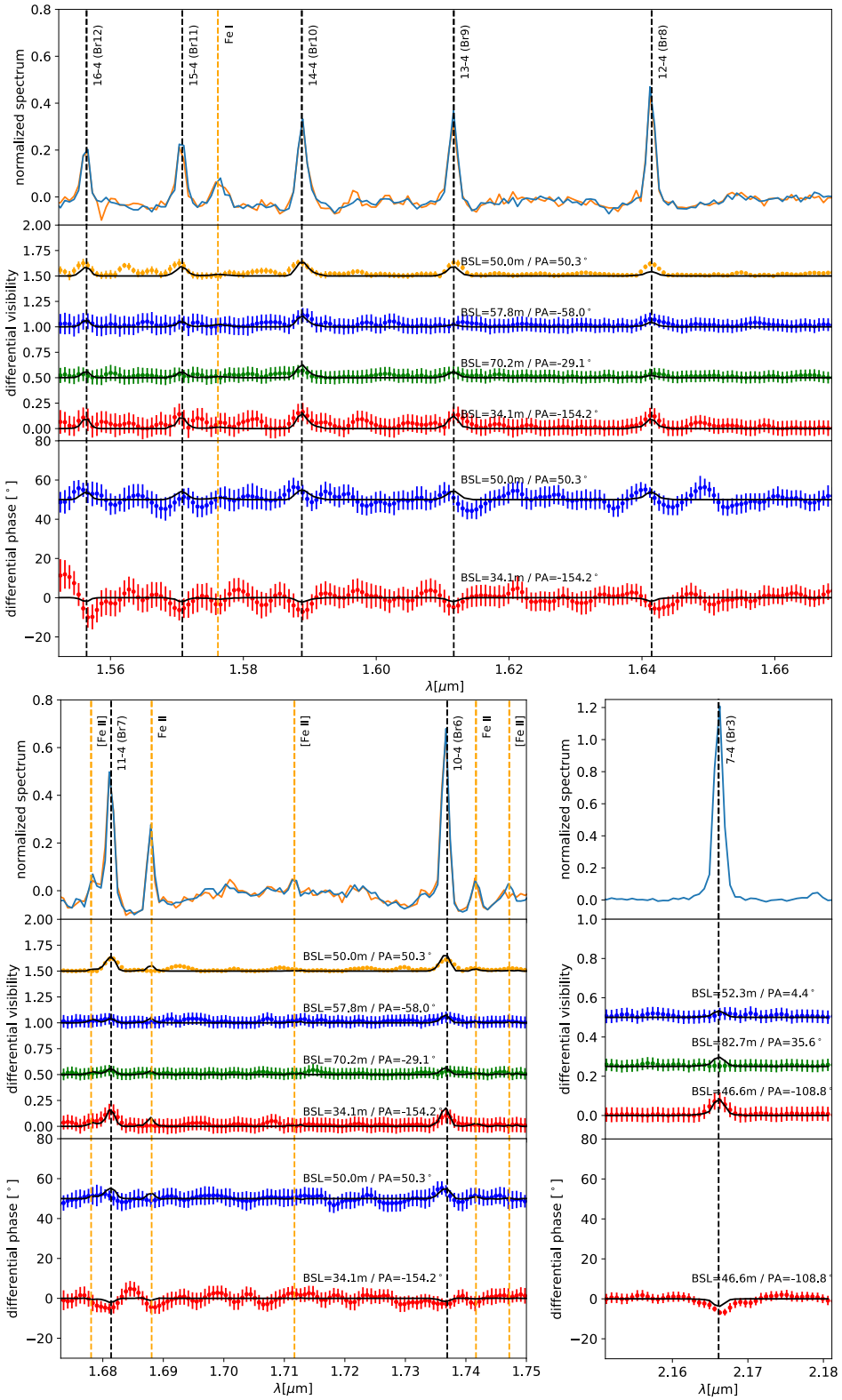

Figure 2. AMBER medium resolution H- and K-band data of V921 Sco (data points with errorbars). The different baselines and position angles are indicated with different colors. Our geometric model is plotted as black line (see Sect. 3.1 and Table 2). In each panel we show **top:** the normalized spectrum, **middle:** the differential visibilities (with offsets of 0.5), and **bottom:** the differential phases (with offsets of 50°). The top and bottom-left panel shows the higher order Brackett transitions from Br6–Br12 and FeII and forbidden [FeII] lines. We plot both spectra (blue and orange) from the two different H-band medium spectral resolution observations (see Table 1). The bottom-right panel shows the Br3 (known as Brγ) transition at 2.1661μm.

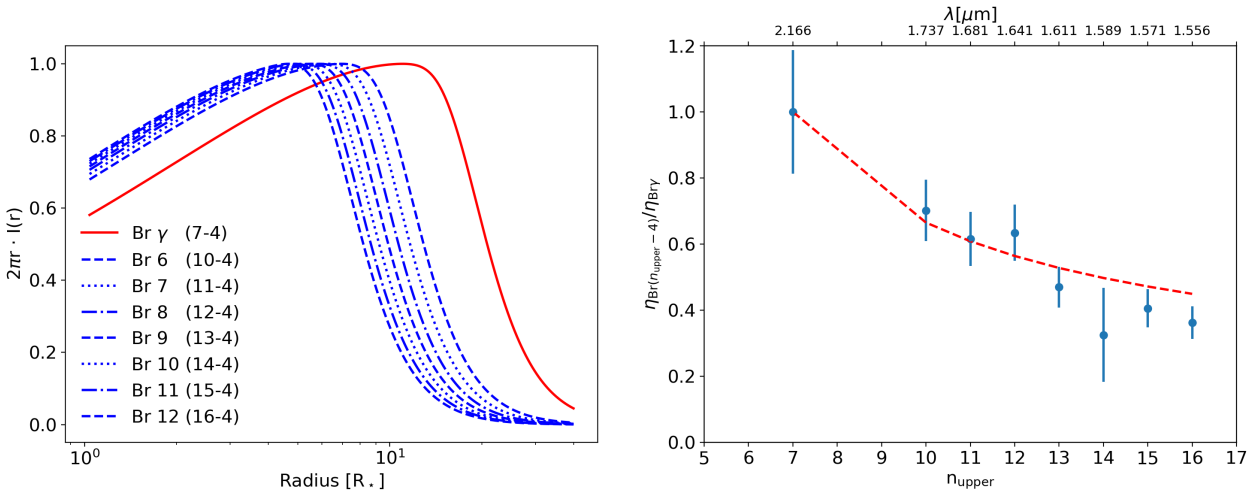

Figure 3. Left: Radial profile of the line transitions Brγ and Br6-Br12, as predicted from our LTE model for V921 Sco (Kraus et al. 2012a). **Right:** Size-ratios of the different line-emitting regions (normalized to the size (η) of the Brγ-line emitting region plotted as blue data points; see Tab. 2). The predicted size-ratios (centroid-ratios; see text) from our LTE model are plotted as dashed red line.

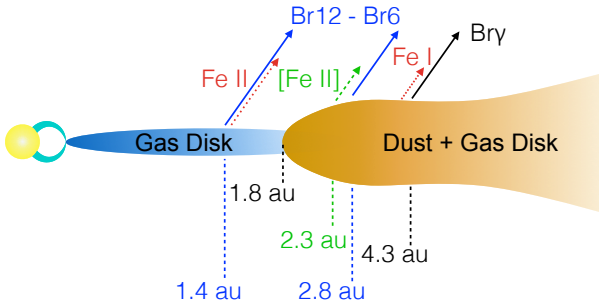

Figure 4. Sketch of the circumstellar disk of V921 Sco A. The different emission line regions are indicated with arrows at their approximate location (see Table 2) from the central star (not to scale).

Table 2. Best-fit parameters of the line visibility fits.

λ [μm]	Transition	η [mas]	η [au]	χ^2_{red}
2.166	Br 3 (Br γ)	3.77 ± 0.10	4.33 ± 0.10	1.18
1.737	Br 6	2.37 ± 0.03	2.72 ± 0.03	1.03
1.681	Br 7	2.32 ± 0.02	2.67 ± 0.02	1.04
1.641	Br 8	2.39 ± 0.11	2.75 ± 0.11	1.04
1.611	Br 9	1.77 ± 0.01	2.03 ± 0.01	1.03
1.589	Br 10	1.23 ± 0.40	1.41 ± 0.40	1.03
1.571	Br 11	1.53 ± 0.15	1.76 ± 0.15	1.02
1.556	Br 12	1.37 ± 0.08	1.58 ± 0.08	1.04
1.576	Fe I	1.89 ± 0.12	2.17 ± 0.12	1.05
1.677	[Fe II]	2.16 ± 0.11	2.48 ± 0.11	1.12
1.687	Fe I	3.17 ± 0.09	3.64 ± 0.09	1.07
1.711	[Fe II]	2.01 ± 0.12	2.31 ± 0.12	1.05
1.741	Fe II	1.52 ± 0.15	1.75 ± 0.15	1.05

the epochs 2009 and 2012 is well in agreement with the prediction of ~28° (with an orbital motion of ~7°/year; Kraus et al. 2012c) assuming a circular orbit.

Geometric model-fitting of different hydrogen lines from Br3–Br12 showed an decrease of the size of the respective line-emitting regions. With a simple radiative transfer model we could show that this decrease is in agreement with LTE conditions of ionised gas located in an equatorial disk. Near-infrared hydrogen emission lines (e.g. the Brackett series) as well as forbidden transitions of e.g. [FeII] trace the ionised components in low density shocked regions (Ninan et al. 2015) of outflows from young stellar objects (Bally 2016). Forbidden lines are also typically observed coming from shock-excited regions in well-collimated jets (Hodapp & Chini 2014; Gardner et al. 2016) or emerging from low-density gas further away within the outflows of young stars (Connelley & Reipurth 2018).

We fitted the approximate size (Gaussian HWHM) of the origin of the Fe I, Fe II and [Fe II] line emission. The forbidden [Fe II] emission arises from ~ 2mas (corresponding to ~2.3au at a distance of 1150pc) region close to the inner disk radius of ~1.6mas (corresponding to ~1.8au at a distance of 1150pc). The Fe I line emission originates from a region between ~ 1.9mas and ~ 3mas whereas the Fe II emission arises from a more compact region (~ 1.5mas, corresponding to ~1.7au at a distance of 1150pc). We illustrate the location of the different emission line regions in Fig. 4.

5 SUMMARY AND CONCLUSION

V921 Sco represents an ideal target to study the different line-emitting regions and the origin of the B[e] phenomenon in detail, due its strong permitted Fe I, Fe II and forbidden [Fe II] line emission (see Fig. 2) and the companion detected in our reconstructed image of the 2008 data (Kraus et al. 2012b).

For the first time higher order Br-lines have been resolved in the circumstellar environment of a B[e] star. The following results can be reported:

- The companion V921 Sco B shows an orbital movement

of ∼ 33° between 2008 and 2012, in agreement with our prediction (Kraus et al. 2012c).

- Our modelling of the H-band visibilities shows that the size of line-emitting region decreases systematically between the Br3 and the Br12 transition. This decrease can be reproduced with a simple radiative transfer model assuming the gas is in LTE conditions and arranged in a circumstellar disk.
- The permitted and forbidden Fe line emission arises from approximately the same location as the dust sublimation region. This could hint to a shock-excitation at the base of an disk wind or outflow.

Better S/R data and sophisticated radiative transfer modelling is required in order to determine whether the high order Brackett lines originate from a Keplerian disk or a disk wind (Tambovtseva et al., submitted; Kreplin et al. 2018; Tambovtseva et al. 2017).
This is the first interferometric study in H-band emission lines and shows the great potential of interferometric H-band observations at a decent spectral resolution. With more and better quality spectrally dispersed H-band interferometric data one will be able not only to constrain the emission sizes of the different hydrogen transitions but also to determine the kinematics as well as the outflow geometry.

ACKNOWLEDGEMENTS

We acknowledge support from an ERC Starting Grant (Grant Agreement No. 639889), STFC Rutherford Fellowship (ST/J004030/1), and STFC Rutherford Grant (ST/K003445/1). This research has made use of NASA's Astrophysics Data System Bibliographic Services. We thank the ESO staff at Paranal for their support during the observations. This work has made use of data from the European Space Agency (ESA) mission *Gaia* (`https://www.cosmos.esa.int/gaia`), processed by the *Gaia* Data Processing and Analysis Consortium (DPAC, `https://www.cosmos.esa.int/web/gaia/dpac/consortium`). Funding for the DPAC has been provided by national institutions, in particular the institutions participating in the *Gaia* Multilateral Agreement.

REFERENCES

Allen D. A., Swings J.-P., 1976, A&A, 47, 293
Arun R., Mathew B., Manoj P., Ujjwal K., Kartha S. S., Viswanath G., Narang M., Paul K. T., 2019, AJ, 157, 159
Bally J., 2016, Annual Review of Astronomy and Astrophysics, 54, 491
Borges Fernandes M., Kraus M., Lorenz Martins S., de Araújo F. X., 2007, MNRAS, 377, 1343
Connelley M. S., Reipurth B., 2018, ApJ, 861, 145
Davis C. J., Whelan E., Ray T. P., Chrysostomou A., 2003, A&A, 397, 693
Gardner C. L., Jones J. R., Hodapp K. W., 2016, ApJ, 830, 113
Gomez de Castro A. I., Pudritz R. E., 1992, Astrophysical Journal, 397, L107
Habart E., Testi L., Natta Vanzi L., 2003, A&A, 400, 575
Henning T., Launhardt R., Steinacker J., Thamm E., 1994, A&A, 291, 546
Hodapp K. W., Chini R., 2014, ApJ, 794, 169
Hutsemekers D., van Drom E., 1990, A&A, 238, 134
Kramida A., Yu. Ralchenko Reader J., and NIST ASD Team 2018, NIST Atomic Spectra Database (ver. 5.6.1), [Online]. Available: `https://physics.nist.gov/asd` [2019, August 20]. National Institute of Standards and Technology, Gaithersburg, MD.
Kraus S., et al., 2012a, ApJ, 744, 19
Kraus S., Calvet N., Hartmann L., Hofmann K.-H., Kreplin A., Monnier Weigelt, Gerd 2012b, ApJ, 746, L2
Kraus S., Calvet N., Hartmann L., Hofmann K.-H., Kreplin A., Monnier Weigelt, Gerd 2012c, ApJ, 752, 11
Kreplin A., Kraus S., Hofmann K.-H., Schertl D., Weigelt G., Driebe T., 2012, A&A, 537, A103
Kreplin A., Madlener D., Chen L., Weigelt G., Kraus S., Grinin V. P., Tambovtseva L., Kishimoto M., 2016, A&A, 590, A96
Kreplin A., Tambovtseva L., Grinin V., Kraus S., Weigelt, Gerd Wang Y., 2018, MNRAS, 476, 4520
Lamers H. J. G. L. M., 2006, Stars with the B[e] Phenomenon. ASP Conference Series, 355, 371
Mannings V., 1994, MNRAS, 271, 587
Merrill P. W., 1928, Astrophysical Journal, 67, 391
Merrill P. W., Burwell C. G., 1933, Contributions from the Mount Wilson Observatory / Carnegie Institution of Washington, 471, 1
Miroshnichenko A. S., Bergner Y. K., Mukanov D. B., Shejkina T. A., 1995, Ap&SS, 224, 519
Miroshnichenko A. S., et al., 2007, ApJ, 671, 828
Muzerolle J., Hartmann L., Calvet N., 1998, AJ, 116, 455
Newville M., Stensitzki T., Allen D. B., Ingargiola A., 2014, LMFIT: Non-Linear Least-Square Minimization and Curve-Fitting for Python, doi:10.5281/zenodo.11813, `https://doi.org/10.5281/zenodo.11813`
Ninan J., Ojha D. K., Mohan V., 2015, in SALT Science Conference 2015 (SSC2015). p. 69
Petrov R. G., et al., 2007, A&A, 464, 1
Swings J.-P., 1977, The Messenger, 8, 10
Tambovtseva L. V., Grinin V. P., Weigelt G., Schertl D., Hofmann K.-H., Caratti o Garatti A., Garcia Lopez R., 2017, in The B[e] Phenomenon: Forty Years of Studies. Proceedings of a Conference held at Charles University. pp 67–
Tatulli E., et al., 2007, A&A, 464, 29
The P. S., de Winter D., Perez M. R., 1994, A&AS, 104, 315
Weigelt G., et al., 2006, in Proc. SPIE. p. 62682S, doi:10.1117/12.671582

This paper has been typeset from a TEX/LATEX file prepared by the author.